

A Graph-Theoretic Monte Carlo Framework for Comparing Delta Surface Dynamics and Subsurface Structure in Numerical Models and Physical Experiments

Alex Miltenberger¹ · Tapan Mukerji¹ · Jayaram Hariharan² · Paola Passalacqua² · Erik Nesvold^{1,3}

Received: 31 August 2020 / Accepted: 15 August 2021

© International Association for Mathematical Geosciences 2021

Abstract As climate changes and populations grow, a deeper understanding of deltaic surface and subsurface processes will help design sustainable management practices of delta resources. Numerical delta models are useful tools for understanding the relationship between the surface and subsurface, but quantitatively linking surface dynamics to subsurface structures remains difficult. The challenges stem from uncertainty in the numerical model parameters and the selection of informative post-processing metrics. In this work a Monte Carlo- and metric-based probabilistic framework is proposed for testing how well a numerical delta model captures the link between surface dynamics and subsurface structure. Probabilistic analysis of three graph-theoretic metrics describing morphology, morphodynamics, and subsurface structure shows that, at the laboratory scale, certain delta surface features, including channelization and channel stability, are informative of the spatial organization of sediment in the subsurface. Other surface features, such as sheet flows, are less informative. The surface dynamics metrics are also applied to data from a laboratory-scale physical experiment to show key differences in the numerical and experimental surface dynamics. The experimental morphology is more channelized than the numerical model and also undergoes more dramatic morphologic changes. These differences are likely due to a combina-

Supplementary Information The online version contains supplementary material available at https://doi.org/10.1007/s11004-021-09973-7.

Published online: 20 September 2021



Stanford Center for Earth Resources Forecasting, Stanford University, 367 Panama Street, Stanford, CA 94305-2220, USA

Department of Civil, Architectural, and Environmental Engineering, University of Texas at Austin, 301 E. Dean Keeton St., Austin, TX 78712-1085, USA

Department of Energy Resources, University of Stavanger, Stavanger, Norway

tion of numerical model resolution limitations, assumptions in the numerical model physics, and differences in flow field extraction in the numerical model and physical experiment.

 $\textbf{Keywords} \ \ \text{Delta modeling} \cdot \text{Graph theory} \cdot \text{Morphodynamics} \cdot \text{Surface processes} \cdot \\ \text{Monte Carlo}$

1 Introduction

Over 300 million people throughout the world live on river deltas (Giosan et al. 2014; Edmonds et al. 2020). Deltas are attractive places for societies because of the abundant water resources, rich soils for agriculture, and a great amount of biodiversity and natural beauty (Hoitink et al. 2020). Understanding the spatiotemporal evolution of deltas and the interactions between the surface processes and subsurface structures will be crucial for informed and sustainable deltaic resource management (Haasnoot et al. 2012).

Many numerical models of deltas have been developed for various purposes, including Sedsim for hydrocarbon exploration (Griffiths et al. 2001), Delft3D for coastal engineering (Lesser et al. 2004), 3D-Sedflux for stratigraphic modeling (Stewart and Irina 2002), and more (Overeem et al. 2005). Surface observations are often used to constrain subsurface flow models (Xu et al. 2021) through conceptual or numerical process models (Hariharan et al. 2021) when direct subsurface information is lacking. However, it is difficult to test how accurately these process models are capturing the link between surface dynamics and subsurface structures (Miller et al. 2008). These difficulties stem from the fact that surface dynamics and subsurface structures are calculated through post-processing of numerical model results, rather than being directly predicted. Therefore, establishing a quantitative link between surface dynamics and subsurface structures requires many model realizations, and the link will be specific to the range of model parameters used. Monte Carlo methods can generate many model realizations from a set of parameters, but the range of parameters varies depending on the application. Many numerical delta model parameters, such as grain size and sediment cohesion, are difficult to adequately constrain, even in well-controlled laboratory experiments (Viparelli et al. 2014; Huang et al. 2012). In this work, the question of how to establish a link between emergent surface dynamics and subsurface structures is addressed in a way that accounts for model parameter uncertainty.

Surface dynamics may be broken down into two components: the morphology of a delta and how that morphology changes (morphodynamics). Many metrics exist to quantify delta surface morphology, morphodynamics, and subsurface structure (Liang et al. 2016; Wolinsky et al. 2010; Edmonds et al. 2011; Heckmann et al. 2015). One subgroup of these metrics are graph-theoretic metrics, which are being increasingly used in the geosciences (Phillips et al. 2015; Kang et al. 2015), with applications to delta soil development (Phillips 2011), and flow field topology and transport properties (Tejedor et al. 2015a, b). Graph-theoretic metrics have also been proposed to validate numerical models of braided channel morphology (Connor-Streich et al. 2018). Because these metrics are uniquely able to capture emergent morphologic features on the delta sur-



face (Marra et al. 2014; Tejedor et al. 2015b) and in the subsurface (Nesvold 2019; Hirsch 1999; Thiele et al. 2016a), they are well suited for studying the relationship between surface dynamics and subsurface structure in deltas if a proper framework for making the comparison in the face of parameter uncertainty is developed (Thiele et al. 2016b).

In this work, a framework is presented to (1) quantify the link between surface dynamics and subsurface structure through a numerical model and (2) compare numerically modeled and experimental surface dynamics. The framework uses Monte Carlo methods to account for numerical model parameter uncertainty and graph-theoretic metrics to quantify morphology, morphodynamics, and subsurface structure. The approach is demonstrated using the numerical model DeltaRCM (Liang et al. 2015b) and experimental data from Straub et al. (2015). The three graph-theoretic metrics are applied to all Monte Carlo realizations of DeltaRCM. Cluster and probabilistic analysis is used to determine which surface and subsurface features are most informative of one another. The morphology and morphodynamics metrics are also applied to the physical experiment and compared to the numerical model using dimension reduction techniques. It is important to note that the focus of this work is not to conclude whether or not DeltaRCM can match the physical experiment, but rather what insights can be drawn from a quantitative comparison.

In Sect. 2, an outline the numerical delta modeling, graph fitting procedure, and the Monte Carlo framework for linking surface dynamics to subsurface structure is presented. Section 3 presents the metrics used to quantify surface dynamics, and subsurface structure are discussed. In Sect. 4, the metrics are applied to a Monte Carlo simulation of DeltaRCM and the physical experiment, and a link between surface dynamics and subsurface structure is established. Finally, in Sect. 5, assumptions used in metric calculation, the surface–subsurface link, and the results of the comparison to the physical experiment are discussed.

2 Methods

In this section, an outline of the framework used to compare numerically modeled flow field dynamics to physical experiment dynamics is presented. An overview of this workflow is shown in Fig. 1. The key components of this workflow are the numerical model DeltaRCM, the graph fitting algorithm, the quantification of uncertainty in DeltaRCM, and the linking of surface metrics to subsurface metrics. Below, each of these steps in the workflow are elaborated. Note that for the physical experiment, subsurface data does not exist, motivating the need to predict subsurface structure from a process-based model like DeltaRCM.

2.1 Modeling Deltas with DeltaRCM

DeltaRCM is an open-source reduced-complexity model designed to simulate delta morphodynamics, with an emphasis on delta-plain channel dynamics. While more details can be found in the relevant papers (Liang et al. 2015a, b), the basic operations are described below.



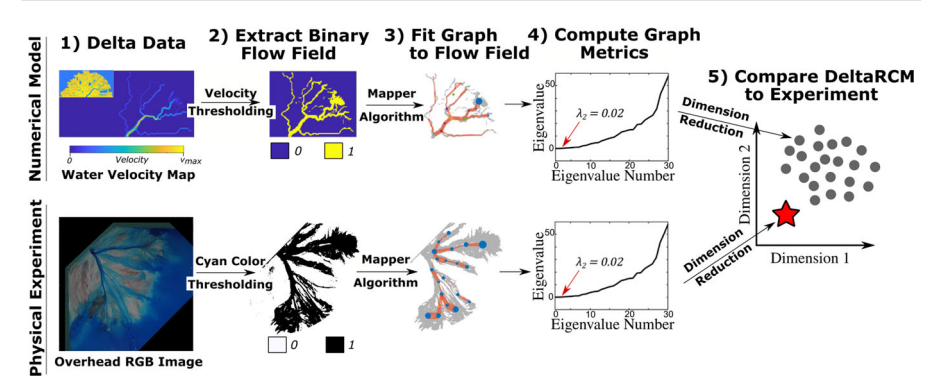


Fig. 1 Workflow for (1–3) fitting graphs to the numerically simulated and experimental deltas and (4–5) comparing the numerical simulations to the physical experiment by extracting quantitative metrics from the flow field graphs

DeltaRCM assumes a rectangular basin with lateral dimensions $w \times \ell$, with grid cell dimensions $\Delta x \times \Delta y$, and a fixed water depth, h_0 . Water and sediment come into the basin through a channel on one side of the domain. Two classes of sediment are considered: mud and sand with their relative proportions controlled by the bedload (sand) fraction f_b . Mud is transported as suspended load and sand is transported as bedload. The quantities of water Q_w and sediment Q_s are then divided into N_w and N_s discrete parcels, respectively. Each parcel is individually routed through the domain using a weighted random walk approach that depends on water depth and the water velocity vector at each pixel along the walk. Sediment erosion and deposition are simulated throughout the random walk using thresholds dependent on the water velocity and sediment type. Once all water and sediment parcels have been routed, the topography, water-free surface, and water velocity are all updated, and the simulation advances in time. A complete list of parameters can be found in Table 1, with more detailed descriptions in Sect. S.1 of the electronic supplementary material (ESM).

2.2 Fitting Graphs to Deltas with the Mapper Algorithm

There are several fundamental ways to represent a graph, but in this work graphs are quantified through the $k \times k$ weighted adjacency matrix, \mathbf{W} , where k is the number of graph nodes. There are several ways to construct \mathbf{W} from delta flow fields, all of which use a binary map of wetted pixels as the main input. This binary map is referred to as a flow field mask because it represents flowing water. The first graphs used to study deltas designated nodes at each channel intersection, with channel segments connecting successive vertices defined as links (Smart 1971). Tejedor et al. (2015a, b) expanded this approach to quantify flow and topological patterns. Several automated procedures, which skeletonize the delta flow field and assign nodes to bifurcation points, have been developed (Schwenk and Hariharan 2021; Marshak et al. 2020). However, sheet flows, commonly observed in physical experiments (Hoyal and Sheets 2009), are not easily skeletonized. Therefore, a different graph abstraction is used for



 Table 1
 DeltaRCM parameters used for the field-scale and Monte Carlo simulations

Parameter	Units	Description	Field-scale value	Monte Carlo value
Q_w	m ³ /s	Inlet water flux	1250	1.72 × 10 ⁻⁴ *
Q_s	kg/s	Inlet sediment flux	1.25	See Table 2 *
$ ho_{\scriptscriptstyle S}$	kg/m ³	Inlet sediment density	1	$2.6348 \times 10^3 **$
SLR	mm/year	Rate of sea level rise	0	See Table 2 *
N_0	_	Number of inlet cells	5	3 [†]
h_0	m	Basin depth	5	$\mathbb{U}(0.1, 0.22)$
N_w	_	Number of water parcels	2000	500 ^{††}
N_{s}	_	Number of sediment parcels	2000	500 ^{††}
$\theta_{m{w}}$	_	Water routing depth dependence exp.	1	$\mathbb{U}(0.5, 1)$
θ_b	-	Bedload routing depth . dependence exp	2	$\mathbb{U}(2,4)$
θ_m	_	Mud routing depth dependence exp.	1	$\mathbb{U}(0.75, 2)$
f_b	-	Input fraction of bedload sediment (sand)	(m) 0.2, (s) 0.8	$\mathbb{U}(0.1, 0.9)$
β	-	Bedload transport capacity exp.	3	$\mathbb{U}(2,3)$
λ	_	Mud deposition quantity coeff.	1	$\mathbb{U}(0.75, 1.25)$
μ_{dm}	-	Mud deposition velocity threshold coeff.	0.3	0.45 **
μ_{em}	-	Mud erosion velocity threshold coeff.	1.5	$\mathbb{U}(1.35, 2)$
μ_{es}	-	Sand erosion velocity threshold coeff.	1.05	$\mathbb{U}(1, 1.25)$
α	_	Topographic diffusion coeff.	0.1	$\mathbb{U}(0.03, 1)$
C_{smooth}	_	Free surface smoothing coeff.	0.9	$\mathbb{U}(0.1, 0.9)$
N_{smooth}	-	Num. free surface smoothing iterations	10	5 ††
ω_{sfc}	-	Water surface underrelaxation coeff.	0.1	$\mathbb{U}(0.01, 0.4)$
ω_{flow}	-	Flow velocity underrelaxation coeff.	0.9	$\mathbb{U}(0.5, 0.99)$
it_{max}	-	Num. flow routing/free sur- face iterations	5	1 ††
γ	_	Flow vector energy partition coeff.	(<i>m</i>) 0.069, (<i>s</i>):0.128	$\mathbb{U}(0.01, 0.1)$
S_0	m/m	Characteristic topographic slope	$(m) 1.4 \times 10^{-4}, (s)$ 2.6×10^{-4}	$\mathbb{U}(1.0 \times 10^{-2}, 5.0 \times 10^{-2})$

 $\mathbb{U}(\cdot,\cdot)$ represents a uniform distribution. (m) and (s) denote to the muddy and sandy field-scale simulations, respectively. *Notes:* *controlled in physical experiment, **held constant for numerical stability, †held constant for geometric consistency, ††held constant to reduce computational time



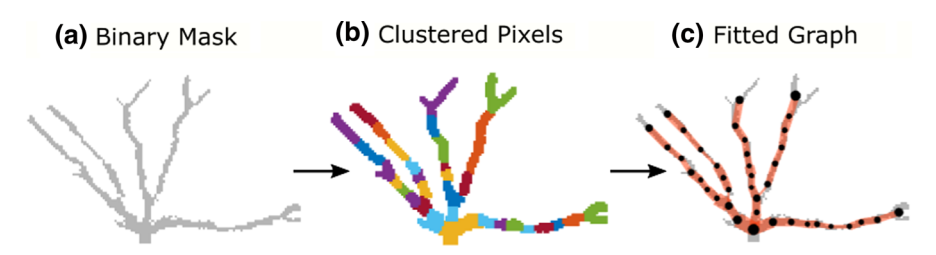


Fig. 2 Mapper algorithm workflow for fitting graphs to binary masks. **a** A binary flow field mask example. **b** Pixels are clustered based on geodesic distances. Each color represents a different cluster of pixels. **c** Graph nodes are assigned to each cluster. Node diameters are proportional to the number of pixels in the node cluster, and edge widths are proportional to the magnitude of the corresponding edge weight in **W**

this work, where nodes represent locations on the flow field that are roughly equidistant from one another, and connections between nodes to represent hydraulic connection (Nesvold 2019). This type of graph, which is better suited for non-channelized flow field morphology, can be fit to a flow field mask automatically using a modified version of the Mapper algorithm from computer science literature (Singh et al. 2007).

2.2.1 The Mapper Algorithm for Fitting Surface and Subsurface Graphs

The modified Mapper algorithm (Nesvold 2019) transforms a binary pixel mask, representing the delta flow field, to a graph. Figure 2 illustrates how the graphs are fit. First, geodesic distances between all pairs of pixels in the mask are computed using the fast marching algorithm (Sethian 1996). Then, pixels are grouped into k clusters based on these geodesic distances using the spectral k-medoids algorithm. Graph nodes represent the medoid of each cluster. Off-diagonal elements of \mathbf{W} are calculated as the inverse of the harmonic mean of geodesic distances to the ten nearest pixels. Therefore, the edge weights represent the connection strength of the two nodes, such that two nodes with larger edge weights have small geodesic distances between them, and vice versa.

The procedure for fitting a graph to a permeability field with the Mapper algorithm is the same as fitting a graph to a flow field mask, except for two key differences. First, a randomly sampled point cloud with *n* points is used as the basis for graph node clustering. Second, eikonal travel times, instead of geodesic distances, are used to calculate distances between the points in the point cloud. The eikonal travel times are computed using the fast marching method (Sethian 1996), with the permeability field used as the speed function. In this way a graph fit to a permeability field represents the dominant subsurface flow pathways.

Both surface and subsurface graphs are affected by the number of desired graph nodes, k. If k is too low, then the stochastic nature of the Mapper algorithm leads to uncertainty in the graph properties of a graph. Increasing k decreases the variability in the spectral properties of the graph, but when k is too large, delta channel networks are indistinguishable by their graph properties (Nesvold 2019). However, the optimal value of k is also a function of the complexity of the delta, with highly branching deltas requiring larger k values. For deltas represented by a 250 \times 250-pixel mask,



Stage	Time (h)	$Q_w \text{ (m}^3\text{/s)}$	Q _s (kg/s)	Base level rise (mm/h)
0	0–127	1.72×10^{-4}	2.65×10^{-4}	0
1	127-478	1.72×10^{-4}	2.65×10^{-4}	0.25
2	478-512	1.72×10^{-4}	3.91×10^{-4}	0
3	512-1481	1.72×10^{-4}	3.91×10^{-4}	0.25

Table 2 Known input parameters for DeltaRCM simulations from TDB-12-1 flume experiment (Straub et al. 2015)

Nesvold (2019) found that k > 50 is best for balancing graph spectrum variability and distinguishing power, and for smaller channel segments $20 \le k \le 50$ is best.

2.2.2 DeltaRCM Flow Field Graphs

To extract the binary flow field mask for graph fitting (Sect. 2.2), the water velocity field simulated by DeltaRCM at a single time step is thresholded. The velocity threshold value is selected so that the flow field mask represents the parts of the delta that are able to entrain sediment (Liang et al. 2016). In practice, a threshold of 0.5 to 1.5 times the mud deposition velocity, u_{dm} , is used. In DeltaRCM, u_{dm} is calculated using the expression $u_{dm} = u_0 \mu_{dm}$ where u_0 is the inlet water velocity and μ_{dm} is the mud deposition coefficient. The inlet velocity is calculated by $u_0 = \frac{Q_w}{N_0 \Delta x h_0}$, where N_0 is the number of inlet cells. A velocity threshold lower than that recommended by Liang et al. (2016) results in an overestimate of sheet flow, and a higher threshold may discard important channels or other parts of the flow field.

The graphs are then fitted to the largest connected component of the binary flow field masks to avoid graph nodes on isolated artifacts produced by the thresholding procedure. Forty graph nodes are used for the field-scale deltas (Sect. 3) and 20 graph nodes for the lab-scale deltas (Sect. 4), in line with the number of nodes that has been shown to be effective for distinguishing delta channel network patterns from one another (Nesvold 2019).

A schematic workflow for this procedure is shown in the top row of Fig. 1. The same procedure is followed for each time step in the DeltaRCM realization after the initialized delta has grown to a point where autogenic dynamics dominate.

2.2.3 DeltaRCM Subsurface Graphs

In DeltaRCM, the subsurface is represented by a three-dimensional spatial field of the sand fraction, $f_s(x, y, z)$. To fit a graph to the subsurface, the sand fraction field must be transformed to a permeability field, k(x, y, z). In this work the transform from sand fraction to permeability is designed to emphasize the fact that, in general, sand is more permeable than mud. It is assumed that a voxel with only mud has a permeability of 10 milliDarcy, and a voxel with only sand has a permeability of 10 Darcy, approximately consistent with permeabilities reported for unconsolidated sediments (Bear 1972).



An exponential transform from sand fraction to permeability under these constraints is shown in the following expression.

$$k(x, y, z) = 0.01 \cdot (1000^{f_s(x, y, z)}).$$
 (1)

After transforming the subsurface sand fraction to permeability, the Mapper algorithm can be used to fit graphs to the permeability field. In this work only the subsurface configuration in the final frame of the DeltaRCM realization is considered in an effort to understand how autogenic variability relates to subsurface observations. As with the flow field graphs, the subsurface graph properties will be sensitive to the number of graph nodes. Nesvold (2019) suggests that subsurface graphs with 50 or more nodes can distinguish differences in subsurface heterogeneity. Therefore, 150 nodes are used in the field-scale simulations (Sect. 3) and 100 nodes in the lab-scale simulations (Sect. 4).

The permeability transform will also affect the subsurface graphs. The permeability transform in Eq. 1 emphasizes the fact that fluid will flow in both sand and mud, but much faster through sand. If the permeability transform did not emphasize the permeability contrast between sand and mud, then all subsurface graphs would be similar. If the permeability transform overemphasized the contrast between sand and mud, then the graph would only represent pockets of sand-dominated material without consideration of flow through mud-dominated material.

2.2.4 Physical Experiment Flow Field Graphs

The physical experiment data used in this study is from the TDB-12-1 experiment, conducted at Tulane University (Straub et al. 2015). A mixture of sand and other types of sediment were fed into a $4.2 \times 2.8 \times 0.65$ -meter basin, using a polymer to simulate sediment cohesion. The experiment consisted of four separate stages, where sediment supply and sea level rise were varied throughout the stages according to Table 2. Data used in this study consist of overhead RGB images taken every 15 minutes and laser topography scans taken every hour. No subsurface data are used in this work, and therefore no subsurface graphs are fit to the physical experiment. Instead, the metric-based relationships calculated using DeltaRCM are used to infer the subsurface characteristics of the physical experiment directly from its surface characteristics.

The binary flow field mask is extracted by detecting water presence in the overhead RGB images. Pixels in each overhead image from TDB-12-1 were classified as wet or non-wet based on the cyan color content, which was shown by Jarriel et al. (2019) to be an effective and straightforward classification scheme. The shoreline is extracted from corresponding laser topography measurements and used to isolate wet pixels on the delta topset, resulting in binary masks of the flow field. Flow field masks are obtained in 1-hour intervals throughout stage 3 (Table 2). Since the automated flow field mask classification was not perfect, 213 frames which upon visual inspection had poor flow field classifications, were manually removed from the physical experiment. On the



remaining 687 flow field masks, graphs are fit to the largest connected component in the mask using 20 nodes, to match the number of nodes used in graphs fitted to Monte Carlo realizations.

2.3 Monte Carlo Framework

Monte Carlo methods are the cornerstone of this framework for comparing numerically modeled deltas to experimental data. This is because many of the DeltaRCM parameters in Table 1 are not explicitly controlled in the physical experiment. The simplest example is the input sand fraction, f_b . The input sediment in TDB-12-1 is a mixture of sand, other sediments, and a cohesive polymer, which cannot be easily separated into sand and mud as required by DeltaRCM. Therefore, the value for f_b is not explicitly controlled by the physical experiment, and a range of f_b values must be tested to see if DeltaRCM is capable of reproducing the experimental surface dynamics. Another 21 DeltaRCM parameters are also not explicitly controlled by the physical experiment (Table 1), prompting the need for Monte Carlo simulations to generate DeltaRCM realizations from the full range of uncertainty in the DeltaRCM parameters.

The Monte Carlo framework for comparing surface dynamics in DeltaRCM to surface dynamics in the experiment consists of five steps. The first step is to define prior distributions for each uncertain DeltaRCM parameter. The second step is to generate many realizations of delta surface and subsurface data by randomly sampling input parameters from the prior distributions. The third step is to calculate metrics for each DeltaRCM realization. The fourth step is to perform cluster and sensitivity analysis on the metrics to understand the trends in the DeltaRCM realizations and which parameters control those trends. The fifth and final step is to compare the metrics calculated for DeltaRCM to those calculated for the physical experiment. These steps are applied in Sect. 4. Then, based on this comparison, inferences about the differences between DeltaRCM and the experiment can be made, and hypotheses for the subsurface structure in the physical experiment can be generated.

2.4 Linking Surface Dynamics to Subsurface Structure

Surface dynamics and subsurface structure are linked through DeltaRCM simulations and a metric- and cluster-driven probabilistic framework. First, metrics that describe surface dynamics and subsurface structure are calculated for each delta in the Monte Carlo simulation. Any set of metrics may be used, but in this work, three graph-theoretic metrics are selected to describe surface dynamics and subsurface structure. These metrics are described in more detail in Sect. 3. Then the models are clustered into three groups based on their corresponding metrics using the k-medoids algorithm. Essentially, each model is mapped to a set of three discrete variables, one variable for morphology, one for morphodynamics, and one for subsurface structure.

Surface dynamics and subsurface structure are then linked through conditional probabilities based on the three clusters each simulated delta is classified into. The probability of any delta being classified into a given cluster is denoted by Pr(class_i),



where $class_i$ represents the event that a delta is classified into cluster i. If a metric has already been observed to be a part of cluster j, then the observation, or condition, is denoted by $cond_j$. Using this notation, the conditional probability of a delta belonging to cluster $class_i$ given the observation $cond_j$ can be calculated from the Monte Carlo realizations using the definition of conditional probability.

$$\Pr(class_i|cond_j) = \frac{\Pr(class_i \cap cond_j)}{\Pr(cond_j)} \qquad \forall i, j \in \{1, \dots, 9\},$$
 (2)

where the numerator and denominator of the right-hand side of (2) can be calculated using indicator functions; in this case, $i, j \in \{1, ..., 9\}$, because the deltas are mapped to three discrete random variables, each with three clusters. Conditional probabilities for all combinations of metrics and clusters can be calculated through Eq. (2) to gain insight on the relationship between metrics.

3 Metrics Describing Surface Dynamics and Subsurface Structure

In this section the metrics that quantify surface dynamics and subsurface structure are described. Surface dynamics are divided into morphology and morphodynamics to separate the shape of the flow field from how the flow field changes throughout time, respectively. Figure 3 illustrates how the DeltaRCM realizations are used to calculate metrics and link them probabilistically. The metrics are illustrated with two simple, synthetic deltas. Both deltas are simulated with DeltaRCM in rectangular 8×4 -km basins, with cell size $\Delta x = 40$ m. All parameters are the same for both realizations except for the bedload fraction f_b , such that one synthetic delta is sand-dominated with higher diffusive forces, and one is mud-dominated with higher inertial forces. The sandy delta uses $f_b = 0.8$, and the muddy delta uses $f_b = 0.2$. The parameters γ and S_0 are calculated as functions of f_b (see Sect. S.1 of the ESM). All of the DeltaRCM parameters are listed in Table 1. Figure 4 shows the evolution of the two simulations throughout 20 years of simulation time with a time step of 29.2 days.

To create the binary flow field mask, the flow velocity is thresholded at 0.7 m/s, about twice the threshold velocity for mud deposition, which for both deltas is 0.375 m/s. Graphs with 40 nodes are then fitted to the largest connected component of the flow field mask. The same procedure is followed for each frame in the DeltaRCM realization, such that each time-series realization is quantified by a set of 250 time steps, each time step with one graph. Since the delta morphology does not stabilize until around 3.5 years into the simulation, only the final 200 graphs are used to compute the morphology and morphodynamics metrics. Subsurface graphs with 150 nodes are fit to the permeability field for each delta computed through Eq. (1).

3.1 Quantifying Flow Field Morphology

Morphologic metrics such as channel fractal dimension, channel width and sinuosity, and wetted area are useful for understanding a delta's flow field (Seybold et al.



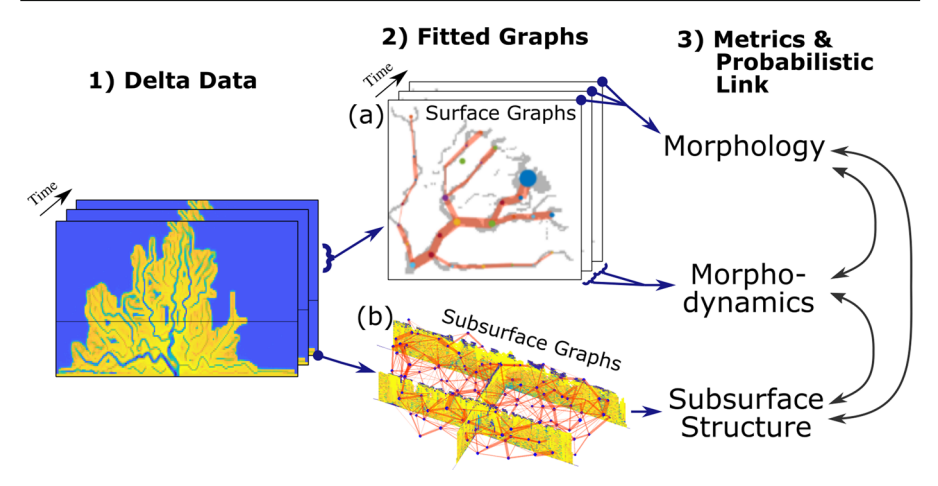


Fig. 3 Workflow illustrating how (1) DeltaRCM data are used to fit (2a) surface graphs to each time step in the DeltaRCM data, and (2b) subsurface graphs to the subsurface data at the final time step. (3) The resulting metrics are linked probabilistically

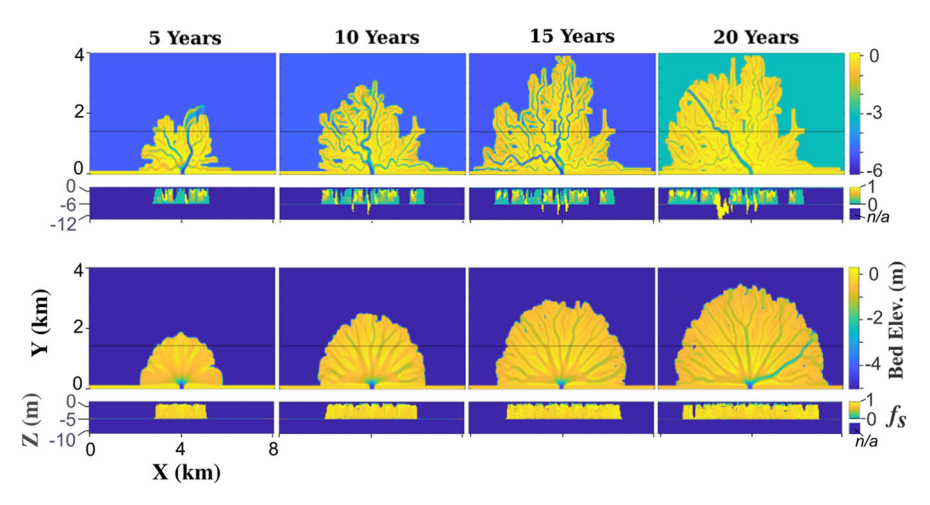


Fig. 4 Snapshots from the two synthetic field-scale deltas created using the default DeltaRCM parameters, except for the sand fraction: (top) 20% bedload fraction and (bottom) 80% bedload fraction

2007; Wolinsky et al. 2010; Liang et al. 2016). However, flow patterns exhibited by laboratory-scale deltas, such as sheet flow, cannot always be easily classified into channels. Similarly, the graph-theoretic metrics proposed by Tejedor et al. (2015b), such as loopiness and resistance distance, rely on the skeletonization of a delta channel network, which is challenging for sheet flow. Therefore, the graph abstraction used by the Mapper algorithm is more useful for quantifying complex flow field geometries exhibited by physical experiments. One graph-theoretic metric that summarizes the shape of a delta flow field, as fitted by the Mapper algorithm, is the algebraic connectivity, or Fiedler value (Fiedler 1973; Chung 1997). The Fiedler value is defined as the first nonzero eigenvalue of the graph Laplacian matrix, and describes the interconnect-



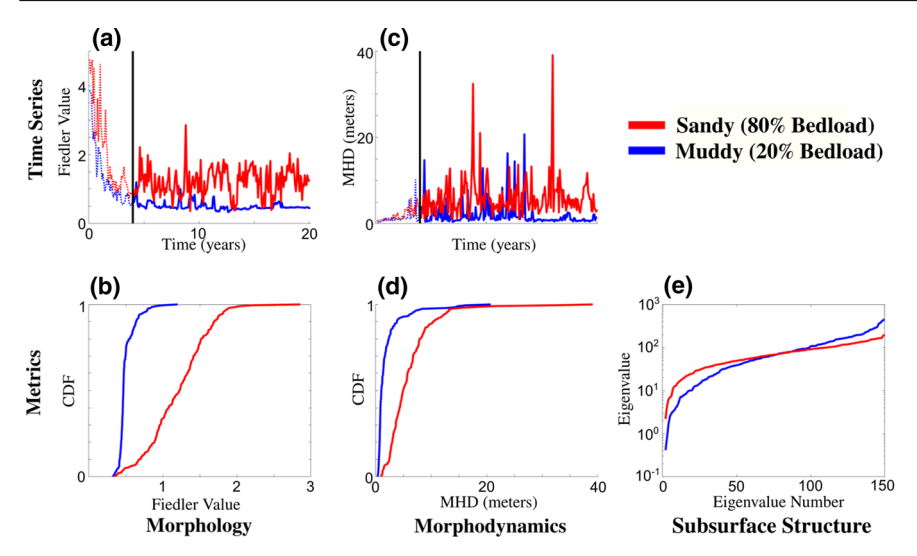


Fig. 5 Time series for a the morphology and c the morphodynamics metrics. b Corresponding CDF metric for morphology and d morphodynamics for the field-scale DeltaRCM realizations. Time steps before the vertical black line (a, c) are not included in the CDFs (b, d). e Permeability Laplacian spectra for the field-scale realizations

edness of nodes in a graph (see Appendix A). In the context of deltas, Phillips (2011) used the Fiedler value to study delta soil development through the spatial connectivity of different soil types. In general, graphs with highly interconnected nodes will have higher Fiedler values than graphs with one or two connections to each node.

3.1.1 Proposed Morphology Metric: the Fiedler Value Cumulative Distribution Function (CDF)

In this work, the Fiedler value is used as the basis for comparing delta flow field morphology because it can be used as a proxy for the degree of channel branching or the presence of sheet flow. To account for temporal variability in the flow field morphology, the CDF of the Fiedler value is estimated using each time step as an individual sample. Flow fields with more branching will have more connections per node and therefore higher average Fiedler values, explaining why the sandy delta has a higher mean Fiedler value than the muddy delta (Fig. 5a,b) and also more branching channels (Fig. 6). Sheet flow will also cause higher Fiedler values for the same reason.

The number of graph nodes and the velocity threshold will significantly affect the magnitude of the Fiedler value. Graphs with more nodes will generally have lower Fiedler values than graphs with fewer nodes. For this reason, the Fiedler value metric is most useful when comparing graphs with equal numbers of nodes. Lower velocity thresholds, which result in more sheet flow-like morphology, will tend to increase the Fiedler value. Higher thresholds, which remove important parts of the flow field, may either decrease the Fiedler value by isolating the main distributary channels, or increase the Fiedler value by removing channels altogether. However, these effects



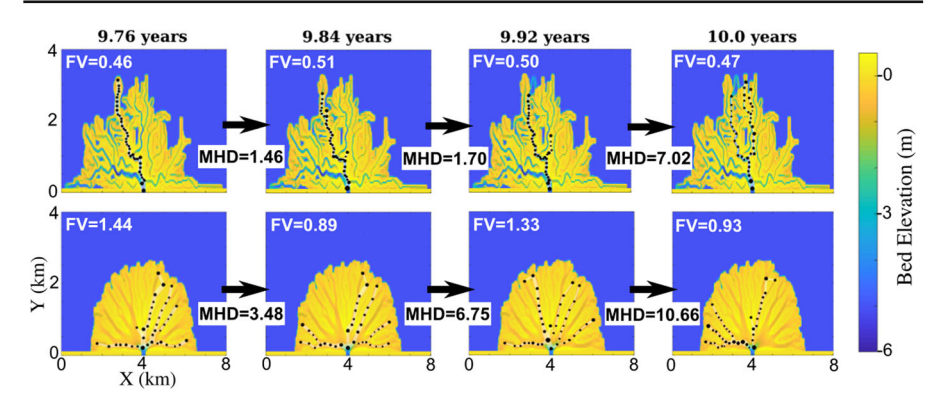


Fig. 6 Example sequence of events in the synthetic field-scale simulation with corresponding Fiedler and MHD values for (top) the 20% bedload simulation and (bottom) the 80% bedload simulation. Flow velocity fields and binary masks can be found in Fig. S2 of the ESM

depend on the specific characteristics of the individual delta and may not hold for all deltas.

3.2 Quantifying Flow Field Morphodynamics

Morphodynamic features such as the avulsion timescale and fluvial reworking timescale (Wickert et al. 2013; Cazanacli et al. 2002; Liang et al. 2016) capture important surface dynamics features, but fail to capture instantaneous changes in the flow field shape. To address this problem, Wickert et al. (2013) use the channel instantaneous planform change metric to quantify the spatial variability of channel networks between two time frames in an experimental delta. Similarly, Scheidt et al. (2016) and Hoffimann et al. (2019) use the modified Hausdorff distance (MHD) to quantify the temporal variability of delta morphology. The MHD was developed to compare shapes in computer vision applications (Dubuisson and Jain 1994; Huttenlocher et al. 1993). The MHD between shape A and shape B is the maximum of two values, d_{AB} and d_{BA} , where d_{AB} is the mean of the set of Euclidean distances between each point on A and the closest point on B, and d_{BA} is the same except between each point on B and the closest point on A. By calculating the MHD between flow fields at successive time steps, Scheidt et al. (2016) and Hoffimann et al. (2019) identify morphodynamic trends that may be used for stochastic modeling.

3.2.1 Proposed Morphodynamics Metric: the Modified Hausdorff Distance CDF

To compare morphodynamics between deltas, the CDF of the MHDs is calculated between successive flow fields to represent the range of morphodynamic variability exhibited by a delta. The MHD calculation is computationally expensive for large numbers of points, so the MHDs are calculated using the graph node locations, instead of the set of points along the edge of the flow field mask, to represent the flow field mask. This modification significantly reduces the dimensionality of the flow field mask



and speeds up the MHD computation. Note that the MHD CDF does not say anything about how a delta is changing, only that relatively large or small changes have occurred between successive time steps. In the synthetic example, the sandy delta, which has a higher mean MHD (Fig. 5b,c), undergoes more rapid channel switching than the muddy delta (Fig. 6).

The MHD CDF will be more sensitive to the velocity threshold than the number of graph nodes, as long as the number of graph nodes is sufficient to cover the entire flow field. If the flow field mask produced by the thresholding procedure overestimates sheet flow, then the MHD will decrease on average because successive sheet flow masks appear similar. If important channels are removed by the thresholding procedure, then the MHD may also decrease, because the flow fields will be more concentrated near the inlet, and channel dynamics will not be captured by the MHD.

3.3 Quantifying Subsurface Flow Structure

Many metrics can be used to quantify the spatial distribution of sediment. Geostatistical metrics like the variogram range and correlation length provide a coarse description of the length scales upon which sedimentary bodies are distributed (Matheron 1963). However, variograms are poor measures of geological connectivity (Mariethoz and Caers 2014), meaning that their ability to identify the degree of preferential flow in the subsurface, an important factor for groundwater and hydrocarbon applications, is limited. Nesvold (2019) proposed using metrics derived from subsurface graphs, fitted using the methods summarized in Sect. 2.2.3, to overcome the inability of variogrambased metrics to describe geological connectivity. In particular, it was shown that the eigenvalue spectrum of the Laplacian matrix can distinguish differences in subsurface structure.

3.3.1 Proposed Subsurface Structure Metric: the Permeability Laplacian Spectrum

The metric describing the subsurface structure is borrowed from Nesvold and Mukerji (2021). The entire eigenvalue spectrum of the subsurface graph Laplacian is used as the subsurface structure metric, and referred to as the permeability Laplacian spectrum. Note that this metric only represents the final state of the subsurface and contains no dynamic information. As an example, the permeability Laplacian spectra of the two synthetic deltas show clear differences, particularly in the lower-order eigenvalues (Fig. 5e). The sandy delta has larger low-order eigenvalues than the muddy delta, including a higher Fiedler value, which corresponds to a highly interconnected subsurface structure (Fig. 7).

The permeability Laplacian spectrum will be predominantly sensitive to the permeability transform. A permeability transform that underemphasizes the contrast between sand and mud will reduce the number of preferential flow pathways and therefore increase the Fiedler value. A permeability transform that overemphasizes the contrast between sand and mud will result in more disconnected flow pathways and a decreased Fiedler value. However, the theory around the higher-order eigenvalues of the Laplacian spectrum is undeveloped (Spielman 2012), and it is unclear how the rest of the



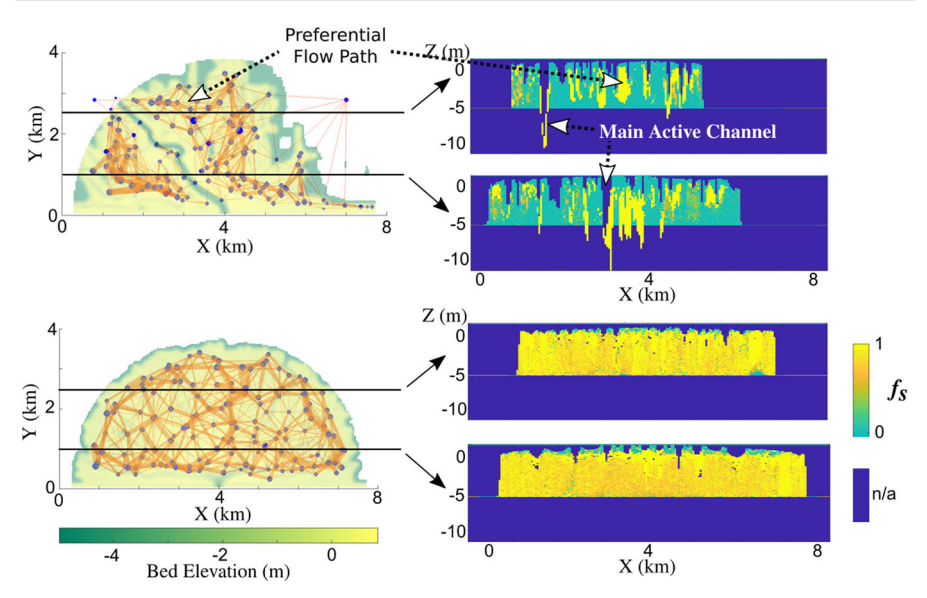


Fig. 7 (Left) Top-down view of the bed elevation field plotted over the three-dimensional permeability field graphs for the (top) 20% bedload and (bottom) 80% bedload deltas. (Right) select cross sections of the sand fraction fields

spectrum is affected by specific differences in subsurface structures and permeability transforms (Nesvold and Mukerji 2021).

4 Linking Surface Dynamics to Subsurface Structure in DeltaRCM and the Physical Experiment

The morphology, morphodynamics, and subsurface structure metrics from Sect. 3 are applied to an ensemble of DeltaRCM realizations generated via Monte Carlo simulation. The eventual goal is to compare the realizations to a physical experiment. Therefore, the Monte Carlo simulation is designed to mimic the physical experiment (Tables 2 and 3). Then, the metrics are calculated and clustered, and sensitivity analyses are performed to interpret the results of the Monte Carlo simulation. Finally, a discussion on how the clusters are related to each other is presented using the probabilistic framework described in Sect. 2.4.

4.1 DeltaRCM Monte Carlo Setup

The Monte Carlo simulation is designed to match the conditions of the physical experiment TDB-12-1 (Sect. 2.2.4) as closely as possible. The spatial and temporal discretization described in Table 3 was used to set up a domain in DeltaRCM that matched the geometry of the experimental basin. The spatial and temporal domains were discretized coarser than the synthetic examples from Sect. 3 to increase numerical stability and reduce computational time. The vertical discretization is a function



Parameter	Description	Value	
\overline{w}	Domain width (x)	4.0 m	
ℓ	Domain length (y)	2.0 m	
N_w	Cells along width	101	
N_ℓ	Cells along length	51	
T	Total simulation time	1481 h	
Δt	Time step	1/3 h	

Table 3 Simulation parameters used in DeltaRCM Monte Carlo runs

of the basin depth, h_0 , such that $\Delta z = 0.1 \cdot h_0$. The temporally varying discharges and base level rise (Table 2) were included as boundary conditions. All other parameters were sampled from the probability distributions in Table 1. The prior distributions represent ranges of numerically stable values, determined by varying parameters one at a time until they caused numerical instabilities in DeltaRCM. In particular, the basin depth, h_0 has a lower bound of 0.1 m that was found to be the lowest value that did not cause numerical instabilities. An upper bound of 0.22 m for h_0 was chosen because the initial water depth of TDB-12-1 was certainly less than a third of the total basin depth of 0.65 m (Straub et al. 2015).

A total of 670 realizations were generated from the Monte Carlo simulation. Snapshots of surface morphology were saved every 8.33 h of simulation time, for a total of 177 snapshots for each realization. Each realization was generated using a set of parameters independently sampled from the distributions in Table 1. Binary flow field masks for each snapshot were created by thresholding the water velocity at 2×10^{-3} m/s, which is about half the velocity required to entrain mud in the DeltaRCM simulations $(2.9 \times 10^{-3} \le u_{dm} \le 4.3 \times 10^{-3}$ m/s). This threshold was determined to produce flow field masks that consistently captured the primary distributary channels without overestimating sheet flow (Fig. S5). Then, graphs with 20 nodes were fit to the binary flow field masks. Permeability field graphs were fit to the subsurface structure at the final time step using 100 nodes and the permeability transform in Eq. (2). The Fiedler value CDFs, MHD CDFs, and permeability Laplacian spectra metrics, described in Sect. 3, were computed for all realizations. The realizations took approximately 583 h to stabilize, and therefore only the final 898 h of simulation time was used in the analysis, leaving a total of 107 morphologic snapshots.

4.2 Linking Morphology, Morphodynamics, and Subsurface Structure through DeltaRCM

Each metric is grouped into three clusters using the k-medoids algorithm. L2-norm distances were used to populate the distance matrices used in clustering. Figure 8 shows all the resulting metrics, colored by cluster.



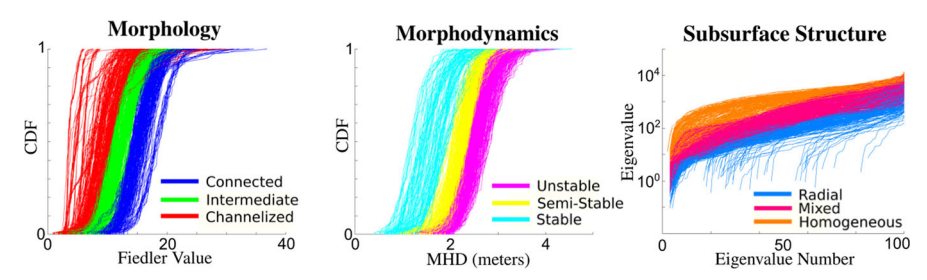


Fig. 8 Summary of the three proposed metrics and clustering results for the Monte Carlo realizations. (left) Fiedler value CDFs, (middle) MHD CDFs, (right) permeability Laplacian eigenvalues, sorted in ascending order

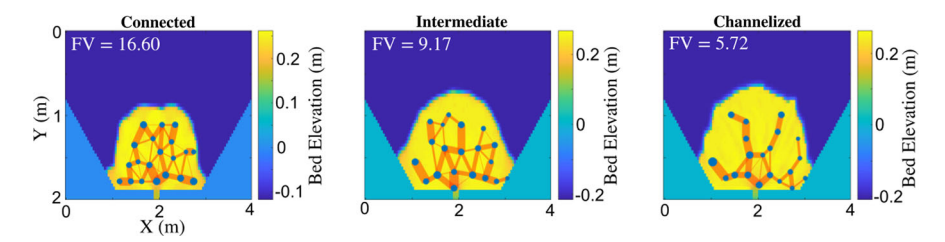


Fig. 9 Bed elevation snapshots with graphs overlain for the morphology medoids taken at hour 1242 of the simulation. Graph nodes are shown as blue dots, and connections are shown in red. Node sizes are proportional to the number of pixels in the node cluster, and edge widths are proportional to the magnitude of the corresponding edge weight in **W**. Flow velocity fields and binary masks can be found in Fig. S3 of the ESM

4.2.1 Cluster Analysis

The morphology clusters in Fig. 9 are separated according to the average Fiedler value of each realization. The term connected will be used to refer to deltas with a high mean Fiedler value, the term channelized will be used to refer to deltas with a low mean Fiedler value, and the term intermediate will be used to refer to deltas somewhere in between. In Fig. 9, the bed elevation and the flow field graphs are plotted for a randomly selected time step. Visual inspection of the graphs in Fig. 9 shows that connected deltas have graphs with more interconnected nodes, channelized deltas have graphs with more of a branching structure, and intermediate deltas are somewhere in between.

The morphodynamics clusters in Fig. 8 are separated according to mean MHD. A delta with a higher mean MHD will be referred to as unstable since the high MHD suggests that the delta experiences larger, more frequent changes. A realization with lower MHDs will be referred to as stable since changes in flow field morphology are smaller. A simulation in between will be referred to as semi-stable. Figure 10 shows time series for the medoid realizations of each morphodynamics cluster. The MHD between each frame is also displayed. The stable delta in Fig. 10 has relatively stable channels that do not move very rapidly. On the other hand, the graph structure for the unstable delta changes more rapidly.



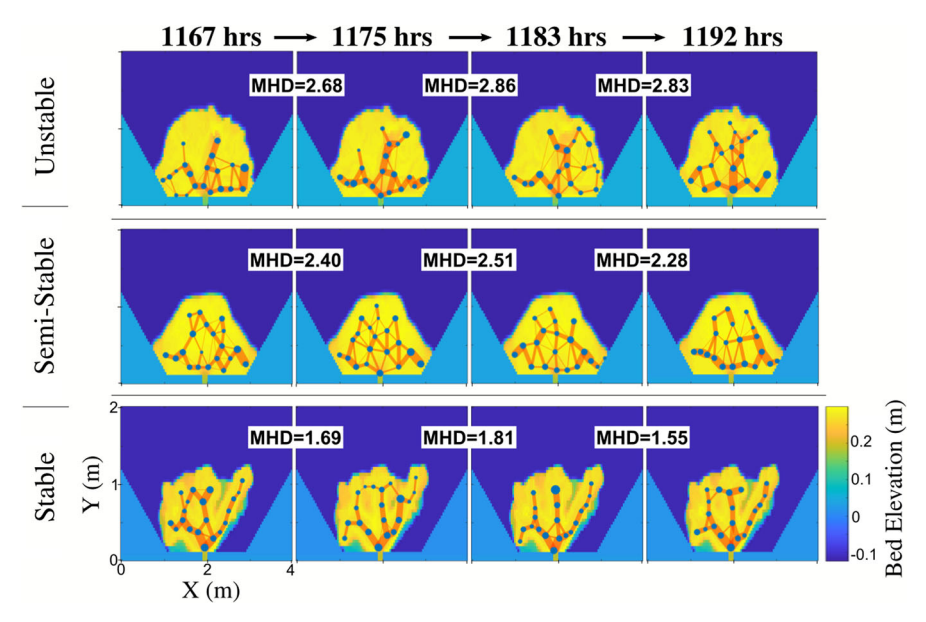


Fig. 10 Four successive snapshots of bed elevation with graphs overlain for the morphodynamics medoids. Node sizes are proportional to the number of pixels in the node cluster, and edge widths are proportional to the magnitude of the corresponding edge weight in \mathbf{W} . Flow velocity fields and binary masks can be found in Fig. S4 of the ESM

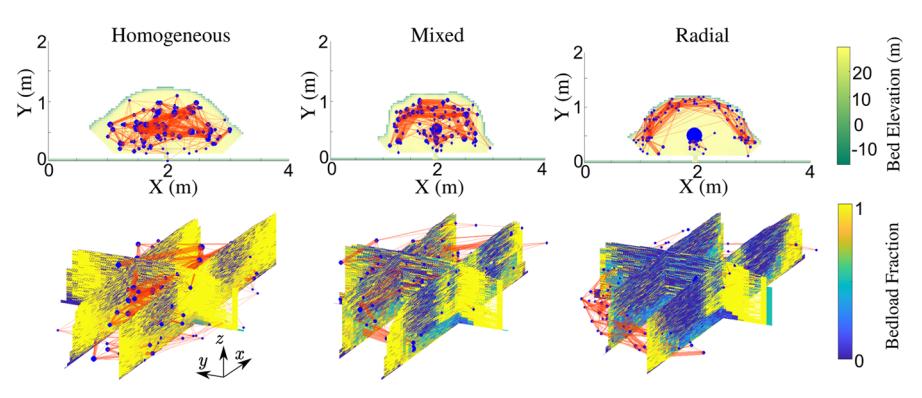


Fig. 11 Medoid stratigraphies for each cluster. (Top) Final bed elevation with stratigraphy graphs overlain. (bottom) Fence diagrams with corresponding graphs

The subsurface structure clusters in Fig. 8 are controlled by the first few eigenvalues in the realization's permeability Laplacian spectrum. The medoid stratigraphies show that subsurface structures with larger eigenvalues have a more interconnected permeability field (Fig. 11), which will be referred to as a homogeneous subsurface structure. Subsurface structures with smaller eigenvalues exhibit a pattern of coarse material concentrated at the apex and the shoreline, which is referred to as a radial subsurface structure. Subsurface structures between the two end members will be referred to as mixed.



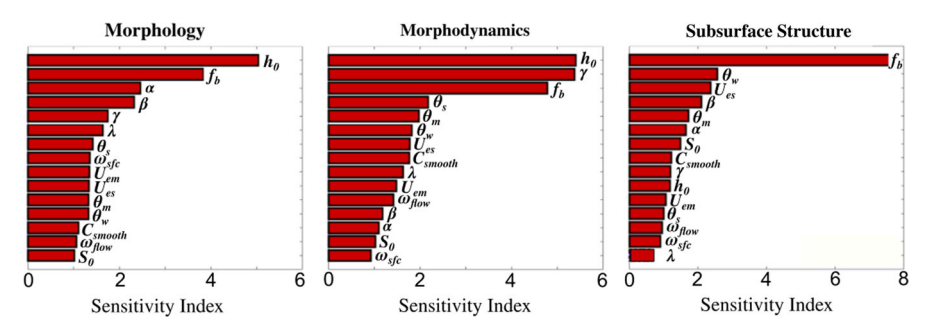


Fig. 12 Pareto charts showing parameter sensitivity analysis results for the metric clusters shown in Fig. 6

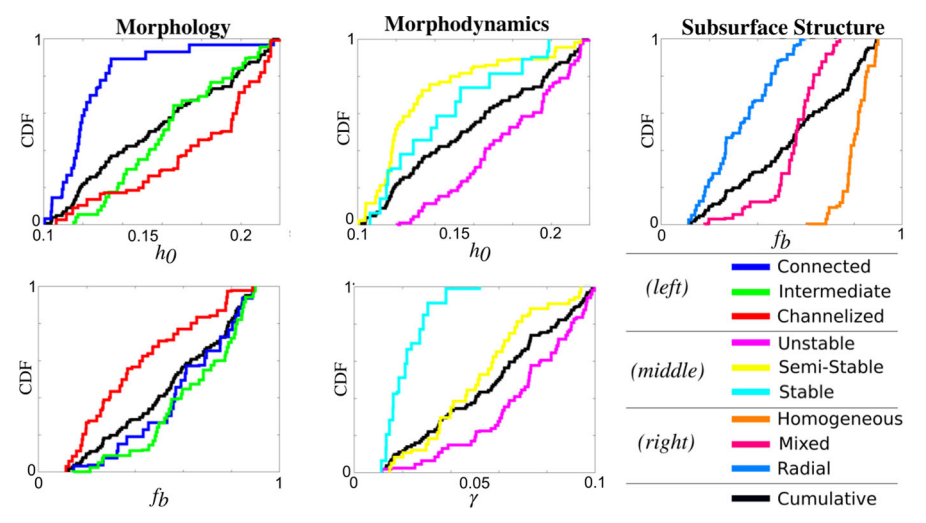


Fig. 13 Conditional cumulative distributions for select metrics, colored by cluster according to the legend in the bottom-right panel

4.2.2 Sensitivity Analysis

Sensitivity analysis is performed using the distance-based generalized sensitivity analysis (DGSA) method (Fenwick et al. 2014). DGSA works by calculating the L2-norm of the difference between the unconditional CDF of an input parameter and the conditional CDFs for the parameters in each cluster. The average differential L2-norm over each of the clusters is normalized by a bootstrapping procedure using samples from the unconditional CDF to estimate a sensitivity index. If the cumulative CDF is significantly different than the conditional CDFs, the sensitivity index will be high, and vice versa. The ten most-sensitive parameters for each type of metric are shown in Pareto charts in Fig. 12. The conditional CDFs of the most sensitive parameters are shown in Fig. 13.

The sand fraction, f_b , is important for all three metrics (Fig. 12). The basin depth, h_0 is also important for both surface dynamics metrics. Finally, the energy partition



coefficient, γ , also plays a significant role in the morphodynamics. A higher f_b is associated with intermediate/connected morphology, unstable morphodynamics, and homogeneous subsurface structures, and vice versa (Fig. 13). Deeper basins are associated with channelized morphology and unstable morphodynamics. Higher γ values, which cause diffusion forces to dominate the flow over inertial forces, are associated with unstable morphodynamics. Lower γ values, where inertial forces dominate the flow, result in more stable morphodynamics.

4.2.3 Conditional Probability Analysis

The conditional probabilities of each cluster combination are computed according to Eq. (2), and are shown in Fig. 14. Four of the nine clusters are strongly informative as conditions, with at least one classification cluster that can be predicted with at least 70% accuracy: connected morphology predicts semi-stable morphodynamics, intermediate morphology predicts unstable morphodynamics, stable morphodynamics predicts channelized morphology and radial subsurface structure, and homogeneous subsurface structure predicts unstable morphodynamics. Morphology in general is not a strong predictor of subsurface structure, and vice versa. Unstable and semi-stable morphodynamics, and radial and mixed subsurface structures, are not very strong predictors of any other cluster.

4.3 Comparing Monte Carlo Realizations to the Physical Experiment

The Fiedler value CDF of the physical experiment is computed from all 687 flow field graphs. For computing MHDs, only successive overhead snapshots that are 8 h apart are considered since DeltaRCM frames were saved every 8.33 h. This left a total of 85 high-quality MHDs that are used to construct the MHD CDF. Finally, a scale correction is applied to ensure that the Fiedler values and MHDs have the same units (meters). Four successive frames with graphs, Fiedler values, and MHDs are shown in Fig. 15.

The experimental and DeltaRCM Fiedler value CDFs and MHD CDFs are plotted in Fig. 16. Multidimensional scaling (Scheidt et al. 2018) is performed with the same distance matrix used for clustering (Sect. 4.2). The metrics in reduced-dimension space are shown in the bottom two panels of Fig. 16. It is clear in Fig. 16 that the experimental graph metrics fall outside the range of those produced by the DeltaRCM realizations. The Fiedler values exhibited by the physical experiment are consistently lower than those exhibited by the DeltaRCM realizations, and the MHDs in the physical experiment have a higher variance than any of the DeltaRCM realizations. However, physical experiment morphology is closest to the channelized group, and the morphodynamics are closest to the unstable group. Varying the flow velocity threshold has little impact on these observations (Figs. S5, S6 of the ESM).



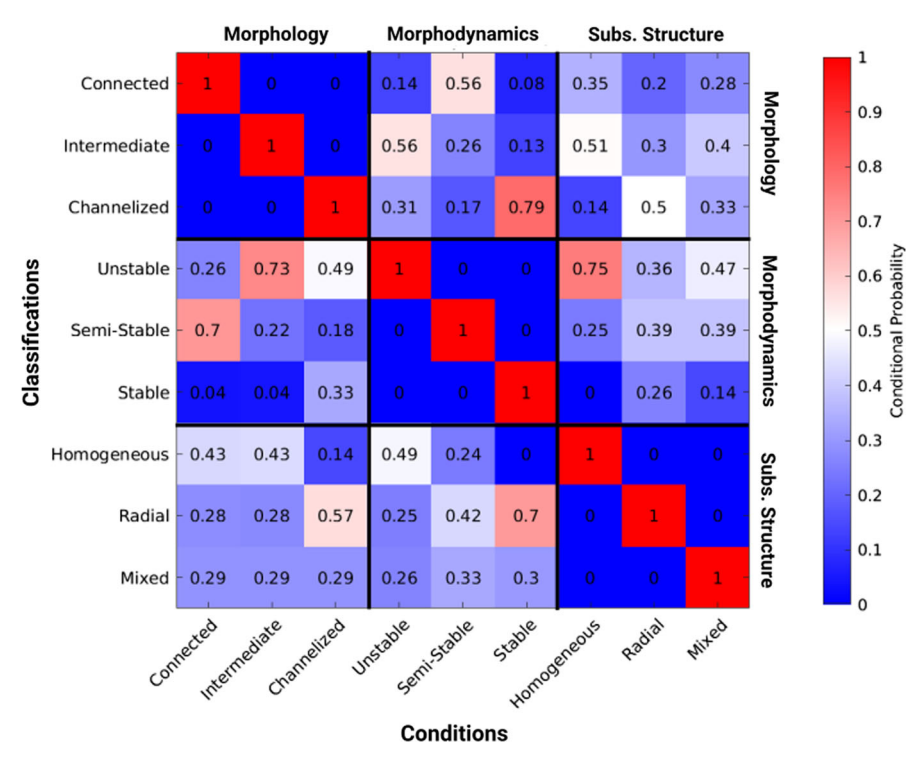


Fig. 14 Conditional probabilities between metric clusters defined by the Monte Carlo simulation. Entries can be read as Pr(Row|Column)

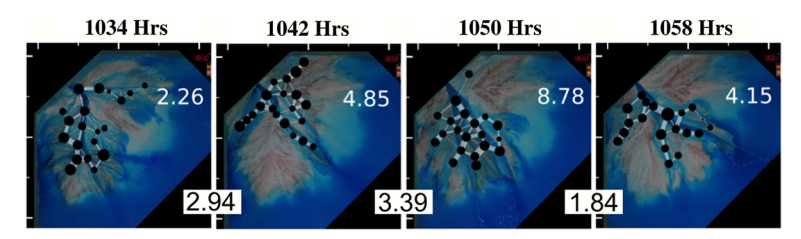


Fig. 15 Four successive time steps from the physical experiment, showing the Fiedler value for each frame in the white text, and the MHD between frames in black text between images. Graph nodes are shown as black dots, and connections are shown in white. Binary masks can be found in Fig. S5 of the ESM

5 Discussion

5.1 Effect of Flow Field Masks on Surface Dynamics Metrics

The flow velocity threshold, required to fit flow field graphs to the DeltaRCM realizations, is a key assumption. Although the velocity threshold is based on the mud deposition velocity (Liang et al. 2016), the mud deposition velocity varies from



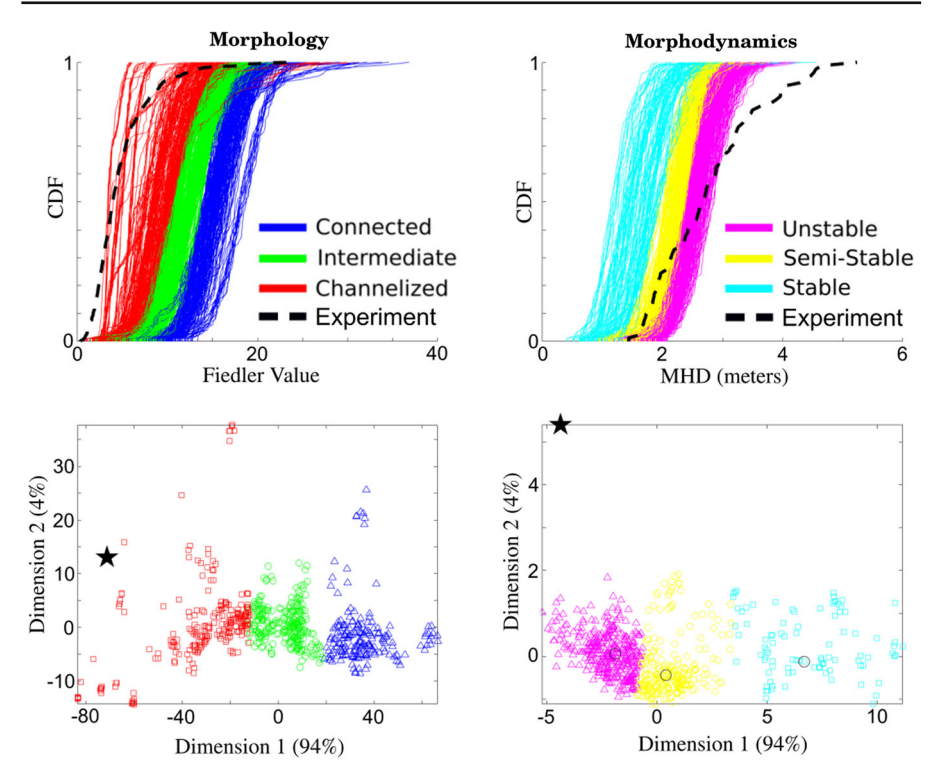


Fig. 16 Comparison of Fiedler value CDF (top left) and MHD CDF (top right) metrics with those derived from the physical experiment. (Bottom) Metrics for all realizations projected into MDS space

 2.9×10^{-3} to 4.3×10^{-3} m/s because of uncertainty in the basin depth. This may explain the sensitivity of the morphology and morphodynamics metrics to the basin depth. The 2.5-mm/s threshold was ultimately chosen because it generally resulted in flow field masks that capture the main distributary channels without overestimating sheet flow. Furthermore, changing the threshold did not significantly affect the comparison to the physical experiment (Fig. S6).

The physical experiment flow field masks depend on the cyan color, not the flow velocity. It is possible that variations in dye color, lighting, and flow depth may affect the quality of the experimental flow field graphs. The fact that the physical experiment flow field masks are not dependent on flow velocity may also have unknown effects on the comparison to DeltaRCM. A more rigorous comparison may use flow depth as a threshold to create DeltaRCM flow field masks as a proxy for the cyan-based experimental flow field masks. However, a flow depth threshold would require accurate, automatic shoreline detection to remove open-water pixels in the DeltaRCM Monte Carlo realizations, e.g. Shaw et al. (2008).



5.2 The Link between Surface Dynamics and Subsurface Structure in DeltaRCM

Conditional probability analysis (Sect. 4.3 and Fig. 14) demonstrates that the link between surface dynamics and subsurface structure is complex. Some features make intuitive sense, such as stable morphodynamics being primarily associated with highly channelized deltas (79%) and homogeneous subsurfaces being formed by unstable morphodynamics (75%). However, the relationships between metrics are not always straightforward. For example, not all informative metrics are bijective; that is, just because one metric informs another metric, does not mean the relationship holds in reverse. For example, stable morphodynamics are predictive of radial subsurface structures (70%), but radial subsurface structures are not predictive of any morphodynamics (26% stable, 39% semi-stable, and 36% unstable). Another feature to note is that some metrics may not be strongly predictive of another metric, but may still be informative by reducing the likelihood of other metrics. For example, a mixed subsurface structure helps to rule out stable morphodynamics (14%), but is less useful for distinguishing between semi-stable (39%) and unstable (47%) morphodynamics. Overall, it is clear that even a highly simplified numerical model such as DeltaRCM can produce complex, nonlinear surface-subsurface relationships.

5.3 Comparing DeltaRCM and Physical Experiment Surface Dynamics and Subsurface Structure

The Fiedler CDF and MHD CDF metrics show that the physical experiment and DeltaRCM produce flow field morphology and morphodynamics in the same order of magnitude, though with some key differences. Generally, the physical experiment is most consistent with channelized morphology and unstable morphodynamics (Fig. 16). However, the morphodynamics exhibited by the physical experiment are significantly different than those of the DeltaRCM realizations. The MHDs in the physical experiment have a much higher variance than any of the DeltaRCM realizations. This implies that the physical experiment experiences morphodynamic changes similar to the magnitude of those in the DeltaRCM realizations some of the time, but at other times undergoes more rapid morphodynamic change than anything observed in the DeltaRCM realizations. The flow field morphology of the physical experiment is slightly more channelized than the DeltaRCM realizations, but much more comparable to DeltaRCM than the morphodynamics metric.

If the morphology and morphodynamics metrics were similar in the experiment and numerical model, then the probabilistic link between surface and subsurface (Fig. 14) could be used to generate a testable hypothesis of the experimental subsurface structure. For example, under the assumption that the physical experiment exhibits channelized morphology, DeltaRCM predicts that the subsurface structure of the physical experiment is most likely radial, with Pr(homo.|chan.) = 0.14, Pr(mixed|chan.) = 0.29, and Pr(radial|chan.) = 0.57. In this hypothetical scenario, one could design a subsurface measurement strategy to test for a radial pattern



of coarse-grained sediment which would indicate whether or not DeltaRCM is able to accurately capture the link between surface dynamics and subsurface structure.

5.4 Discrepancy Between Experimental and DeltaRCM Surface Dynamics

There are several reasons why the physical experiment and DeltaRCM realizations exhibit different surface dynamics. The first reason may be due to the differences in how the flow field masks are calculated. For the numerical deltas, the flow field masks are calculated using a flow velocity threshold, whereas the physical delta flow field masks are calculated by thresholding the cyan saturation in each pixel. The cyan saturation is a complex function of the flow velocity, as well as dye concentration, flow depth, the underlying sediment, and other fluid dynamics phenomena that are not perfectly correlated with the flow velocity. This possibly excludes thin or fast-moving flows from the cyan-based flow field masks and may introduce some bias in the comparison between the numerical and physical deltas.

The second potential reason for the discrepancy between the physical experiment and DeltaRCM realizations is that the physical processes of DeltaRCM are fundamentally different than those in the experiment. For example, DeltaRCM uses only two grain sizes that may not be representative of the full range of sediment and cohesive polymers used in the physical experiment. The sediment transport model of DeltaRCM, which uses two grain sizes, may be inadequate to capture the transport properties of the full range of sediment and cohesive polymers used in the physical experiment.

The final potential reason that DeltaRCM and the physical experiment exhibit different surface dynamics is that the spatial and temporal resolution of the DeltaRCM simulations is too coarse. Previous work has shown that capturing the fine-scale channel dynamics is important for modeling deltas (Tucker and Hancock 2010). If the resolution were increased and resulted in less sheet flow, then the Fiedler values would decrease and the MHDs would increase, which would be more similar to the physical experiment. To test this hypothesis, significant development of the DeltaRCM code is required to reduce the number of errors the simulation encounters before a Monte Carlo analysis is feasible. In this work, 36% of realizations failed before completion. The failure rate increases dramatically as spatial and temporal resolution increases. The significant number of failures are thought to be influenced primarily by unstable parameter combinations and random errors in the stochastic routing algorithm. Ongoing improvements to DeltaRCM (Moodie et al. 2021) will make future Monte Carlo studies more practical for higher-resolution models.

6 Conclusions

Emergent deltaic surface dynamics characteristics in numerical models are quantitatively compared to those observed in a physical experiment using a Monte Carlo and metric-based framework. Using graph-theoretic metrics to describe delta flow field morphology, morphodynamics, and subsurface structure, the experimental delta is shown to exhibit more channelized flow field morphologies and a wider range of morphodynamic behavior than what was simulated in DeltaRCM.



More work is needed to determine the effect of the flow velocity threshold, used to create flow field masks for graph fitting, on the metrics used in the comparison. Other metrics may also be used to study other emergent relationships in the numerical model. Improving the numerical stability of DeltaRCM at higher spatial and temporal resolutions may also impact the modeled surface dynamics and subsurface structure. Regardless, using Monte Carlo simulations to account for model parameter uncertainty in the comparison of numerical models and physical experiments provides deeper insight into the limitations of numerical models to capturing deltaic surface dynamics, and helps generate testable hypotheses for how surface dynamics relates to subsurface structure in natural systems.

Acknowledgements The authors would like to acknowledge the Stanford Center for Earth Resources Forecasting and the Dean of the Stanford School of Earth, Energy, and Environmental Sciences, Prof. Steve Graham, for providing funding. The National Science Foundation (grant EAR-1719670) helped support this research on the link between surface and subsurface processes. The authors also thank Prof. Kyle Straub for providing the TDB-12-1 experiment data and feedback on quantifying experimental results. The authors also thank Prof. Alejandro Tejedor for the feedback which greatly improved this manuscript.

Appendix A: Graph Theory and the Fiedler Value

Graph theory is a mathematical description of a set of nodes linked together by edges (Chung 1997). The nodes and edges can have different interpretations for different applications, but share a common mathematical framework. One way to represent a graph with k nodes is through a $k \times k$ symmetric matrix \mathbf{W} called the weighted adjacency matrix. The diagonal elements of \mathbf{W} are zeros. Off-diagonal elements of \mathbf{W} , denoted by W_{ij} , are zero if nodes i and j are not connected, and some positive value if the nodes are connected.

An important property of a weighted graph is the graph Laplacian matrix L. The graph Laplacian is defined as L = D - W, where

$$\mathbf{D} = \operatorname{Diag}(d_1, d_2, \dots, d_k)$$

$$d_i = \sum_{i=1}^k W_{ij}.$$
(3)

The graph Laplacian is important because its eigenvalue spectrum contains a measure of the topological connectivity of the graph. For a graphs without disconnected components, the first eigenvalue, λ_1 , of the Laplacian matrix is zero. The second eigenvalue, λ_2 , is called the Fiedler value, or algebraic connectivity. The Fiedler value is a scalar measure of the interconnectedness of a graph. By definition, the Fiedler value must satisfy the following optimization problem, where b_i is the i^{th} element of the second eigenvector of \mathbf{L} , \mathbb{E} is the set of all edges in the graph, and \mathbb{V} is the set of all nodes (Chung 1997).



$$\lambda_2 = \min_{\mathbf{b}} \frac{\sum_{(i,j) \in \mathbb{E}} (b_i - b_j)^2 W_{ij}}{\sum_{i \in \mathbb{V}} b_i^2 d_i}$$
s.t.
$$\sum_{i=1}^n b_i d_i = 0$$
(4)

If the nodes of a graph have few connections, then there will be fewer edges in \mathbb{E} . With fewer edges in \mathbb{E} , the numerator of (4) will be small relative to the denominator. Therefore, for a graph containing nodes with few connections, λ_2 will be small. By the same reasoning, a graph containing nodes with many connections will have a large λ_2 . In this way the Fiedler value quantifies, on average, how interconnected the nodes of a graph are.

References

Bear J (1972) Dynamics of fluids in porous media. Dover, ISBN 978-0-486-65675-5

Cazanacli D, Paola C, Parker G (2002) Experimental steep, braided flow: application to flooding risk on fans. J Hydraul Eng 128(3):322–330

Chung FR (1997) Spectral graph theory. American Mathematical Society

Connor-Streich G, Henshaw AJ, Brasington J, Bertoldi W, Harvey GL (2018) Let's get connected: a new graph theory-based approach and toolbox for understanding braided river morphodynamics. WIREs Water 5(5):e1296

Dubuisson MP, Jain AK (1994) A modified hausdorff distance for object matching. In: Proceedings of 12th international conference on pattern recognition 1:566–568

Edmonds DA, Caldwell RL, Brondizio ES, Siani SMO (2020) Coastal flooding will disproportionately impact people on river deltas. Nat Commun 11(1):4741. ISSN 2041-1723

Edmonds DA, Paola C, Hoyal DCJD, Sheets BA (2011) Quantitative metrics that describe river deltas and their channel networks. J Geophys Res: Earth Surf, 116

Fenwick D, Scheidt C, Caers J (2014) Quantifying asymmetric parameter interactions in sensitivity analysis: application to reservoir modeling. Math Geosci 46:493–591

Fiedler M (1973) Algebraic connectivity of graphs. Czechoslov Math J 23(2):298-305

Giosan L, Syvitski J, Constantinescu S, Day J (2014) Climate change: protect the world's deltas. Nature 516:31–33

Griffiths C, Dyt C, Paraschivoiu E, Liu K (2001) Sedsim in hydrocarbon exploration. In: Merriam D, Davis J (eds) Geologic modeling and simulation. computer applications in the earth sciences. Springer, Boston, MA, ISBN 978-1-4615-1359-9

Haasnoot M, Middelkoop H, Offermans A, van Beek E, van Deursen WP (2012) Exploring pathways for sustainable water management in river deltas in a changing environment. Clim Change 115:795–819

Hariharan J, Xu Z, Michael HA, Paola C, Steel E, Passalacqua P (2021) Linking the surface and subsurface in river deltas - part 1: relating surface and subsurface geometries. Water Resources Research accepted:e2020WR029282, e2020WR029282 2020WR029282

Heckmann T, Schwanghart W, Phillips J D (2015) Graph theory–recent developments of its application in geomorphology. Geomorphology 243:130–146, ISSN 0169-555X

Hirsch L (1999) Graph theory applications to continuity and ranking in geologic models. Comput Geosci 25(2):127–139 (ISSN 0098-3004)

Hoffimann J, Bufe A, Caers J (2019) Morphodynamic analysis and statistical synthesis of geomorphic data: application to a flume experiment. J Geophys Res Earth Surf 124(11):2561–2578

Hoitink A, Nittrouer J, Passalacqua P, Shaw J, Langendoen E, Huismans Y, van Maren D (2020) Resilience of river deltas in the anthropocene. J Geophysi Res: Earth Surf 125(3)

Hoyal DCJD, Sheets BA (2009) Morphodynamic evolution of experimental cohesive deltas. J Geophys Res: Earth Surf 114(F2)



- Huang X, Dyt C, Griffiths C, Salles T (2012) Numerical forward modelling of fluxoturbidite flume experiments using sedsim. Mar Petrol Geol 35(1):190–200
- Huttenlocher DP, Klanderman GA, Rucklidge WJ (1993) Comparing images using the hausdorff distance. IEEE Trans Pattern Anal Mach Intell 15(9):850–863
- Jarriel T, Isikdogan LF, Bovik A, Passalacqua P (2019) Characterization of deltaic channel morphodynamics from imagery time series using the channelized response variance. J Geophys Res: Earth Surf 124(12)
- Kang S, Bhark E, Datta-Gupta A, Kim J, Jang I (2015) A hierarchical model calibration approach with multiscale spectral-domain parameterization: application to a structurally complex fractured reservoir. J Petrol Sci Eng 135:336–351, ISSN 0920-4105
- Lesser G, Roelvink J, van Kester J, Stelling G (2004) Development and validation of a three-dimensional morphological model. Coast Eng 51(8):883–915, ISSN 0378-3839, coastal Morphodynamic Modeling
- Liang M, Geleynse N, Edmonds D, Passalacqua P (2015a) A reduced-complexity model for river delta formation—part 2: assessment of the flow routing scheme. Earth Surf Dyn 3(1):87–104
- Liang M, van Dyk C, Passalacqua P (2016) Quantifying the patterns and dynamics of river deltas under conditions of steady forcing and relative sea level rise. J Geophys Res: Earth Surf 121(2)
- Liang M, Voller V, Paola C (2015b) A reduced-complexity model for river delta formation—part 1: modeling deltas with channel dynamics. Earth Surf Dyn 3(1):67–86
- Mariethoz G, Caers J (2014) Multiple-point geostatistics: stochastic modeling with training images. Wiley, ISBN 9781118662953
- Marra WA, Kleinhans MG, Addink EA (2014) Network concepts to describe channel importance and change in multichannel systems: test results for the Jamuna River, Bangladesh. Earth Surf Proc Land 39(6):766–778
- Marshak C, Simard M, Denbina M, Nilsson J, Van der Stocken T (2020) Orinoco: Retrieving a river delta network with the fast marching method and python. ISPRS Int J Geo-Inf 9(11), ISSN 2220-9964
- Matheron G (1963) Principles of geostatistics. Econ Geol 58(8):1246–1266. ISSN 0361-0128
- Miller JK, Sun T, Li H, Stewart J, Genty C, Li D, Lyttle C (2008) Direct Modeling of Reservoirs through Forward Process-based Models: Can We Get There? volume All Days of IPTC International Petroleum Technology Conference, iPTC-12729-MS
- Moodie AJ, Hariharan J, Barefoot E, Passalacqua P (2021) *pyDeltaRCM*: a flexible numerical delta model. J Open Source Softw 6(64):3398. https://doi.org/10.21105/joss.03398
- Nesvold E (2019) Building informative priors for the subsurface with generative adversarial networks and graphs. Ph.D. thesis, Stanford University
- Nesvold E, Mukerji T (2021) Mapping of connectivity properties in heterogeneous porous media with graphs. Math Geosci Under review
- Overeem I, Syvitski JP, Hutton EW (2005) Three-dimensional numerical modeling of deltas. SEPM (Society for Sedimentary Geology), ISBN 1-56576-113-8, sEPM Special Publication No. 83
- Phillips JD (2011) Predicting modes of spatial change from state-and-transition models. Ecol Model 222(3):475–484 (ISSN 0304-3800)
- Phillips JD, Schwanghart W, Heckmann T (2015) Graph theory in the geosciences. Earth-Sci Rev 143:147–160. ISSN 0012-8252
- Scheidt C, Fernandes AM, Paola C, Caers J (2016) Quantifying natural delta variability using a multiplepoint geostatistics prior uncertainty model. J Geophys Res: Earth Surf 121(10)
- Scheidt C, Li L, Caers J (2018) Quantifying uncertainty in subsurface systems. Wiley, ISBN 978-1-119-32583-3
- Schwenk J, Hariharan J (2021) Rivgraph: automatic extraction and analysis of river and delta channel network topology. J Open Source Softw 6(59):2952
- Sethian JA (1996) A fast marching level set method for monotonically advancing fronts. Proc Natl Acad Sci 93(4):1591–1595. ISSN 0027-8424
- Seybold H, Andrade JS, Herrmann HJ (2007) Modeling river delta formation. Proc Natl Acad Sci 104(43):16804–16809. ISSN 0027-8424
- Shaw JB, Wolinsky MA, Paola C, Voller VR (2008) An image-based method for shoreline mapping on complex coasts. Geophys Res Lett 35(12)
- Singh G, Mémoli F, Carlsson G (2007) Topological methods for the analysis of high dimensional data sets and 3d object recognition. In: Botsch M, Pajarola R, Chen B, Zwicker M (eds) Eurographics symposium on point-based graphics. The Eurographics Association, ISBN 978-3-905673-51-7, ISSN 1811-7813



- Smart J (1971) Quantitative properties of delta channel networks. Technical Report 3, IBM Thomas J. Watson Research Center
- Spielman D (2012) Spectral graph theory. In Combinatorial Scientific Computing, chapter 16
- Stewart J, Irina O (2002) 3d-sedflux; coupling fluvial and stratigraphic simulation models
- Straub KM, Li Q, Benson WM (2015) Influence of sediment cohesion on deltaic shoreline dynamics and bulk sediment retention: a laboratory study. Geophys Res Lett 42(22):9808–9815
- Tejedor A, Longjas A, Zaliapin I, Foufoula-Georgiou E (2015a) Delta channel networks: 1. A graph-theoretic approach for studying connectivity and steady state transport on deltaic surfaces. Water Resour Res 51(6):3998–4018
- Tejedor A, Longjas A, Zaliapin I, Foufoula-Georgiou E (2015b) Delta channel networks: 2. metrics of topologic and dynamic complexity for delta comparison, physical inference, and vulnerability assessment. Water Resour Res 51(6):4019–4045
- Thiele ST, Jessell MW, Lindsay M, Ogarko V, Wellmann JF, Pakyuz-Charrier E (2016a) The topology of geology 1: topological analysis. J Struct Geol 91:27–38. ISSN 0191-8141
- Thiele ST, Jessell MW, Lindsay M, Wellmann JF, Pakyuz-Charrier E (2016b) The topology of geology 2: topological uncertainty. J Struct Geol 91:74–87. ISSN 0191-8141
- Tucker GE, Hancock GR (2010) Modelling landscape evolution. Earth Surf Proc Land 35(1):28-50
- Viparelli E, Blom A, Ferrer-Boix C, Kuprenas R (2014) Comparison between experimental and numerical stratigraphy emplaced by a prograding delta. Earth Surf Dyn 2(1):323–338
- Wickert AD, Martin JM, Tal M, Kim W, Sheets B, Paola C (2013) River channel lateral mobility: metrics, time scales, and controls. J Geophys Res: Earth Surf 118(2):396–412
- Wolinsky MA, Edmonds DA, Martin J, Paola C (2010) Delta allometry: growth laws for river deltas. Geophys Res Lett 37(21)
- Xu Z, Hariharan J, Passalacqua P, Steel E, Paola C, Michael HA (2021) Linking the surface and subsurface in river deltas—part 2: relating subsurface geometry to groundwater flow behavior. Water Resour Res. Accepted:e2020WR029281, e2020WR029281 2020WR029281

